Cylindrical Domains of Block Copolymers Developed via Ordering under Moving Temperature Gradient

Kazuki Mita,[†,§] Hirokazu Tanaka,[†,§] Kenji Saijo,[†] Mikihito Takenaka,[†] and Takeji Hashimoto*[,†,‡,#]

Department of Polymer Chemistry, Graduate School of Engineering, Kyoto University, Katsura, Nishikyo-ku, Kyoto 615-8510, Japan, and Advanced Science Reserch Center (ASRC), Japan Atomic Energy Agency (JAEA), Tokai-mura, Ibaraki-Pref. 319-1195, Japan

Received February 15, 2007; Revised Manuscript Received May 21, 2007

ABSTRACT: A zone heating method, which imposes the moving temperature-gradient (∇T) field on ordering process of various melts in general, enabled to control a macroscopic orientation of microdomain structures in block copolymer bulk. We applied the method to a polystyrene-*block*-polyisoprene diblock copolymer forming hexagonally packed cylindrical domains (hex−cyl) in the absence of external fields. We discovered that the method creates the following special texture of hex−cyl: (1) The texture seemingly consists of volume-filled columnar grains with the grain axis parallel to the ∇T axis (defined as the O*z* axis). (2) The cylinder axis always orients perpendicular to the O*z* axis with a rotational angle ϕ of the cylinder axis around the O*z* axis being fixed within a grain but statistically varying randomly among different grains. (3) One set of the (100) plane of hex−cyl preferentially oriented perpendicular to O*z* axis with a small rotational degree of freedom around the cylinder axis. We interpret that the special texture is a consequence of the surface-induced order−disorder transition of the block copolymer under the moving ∇T field.

1. Introduction

Bulk block copolymers (bcps) form ordered microdomain structures which have various symmetries with nanoperiodicity.[1] Moreover, the microdomain structures themselves have intrinsic anisotropy. However, the bulk bcps are composed of small grains impinged to each other at the grain boundaries, and the intrinsic anisotropy which exists within the grain is averaged out over an orientation distribution of the grains. Therefore, to take a full advantage of the intrinsic anisotropy of ordered microdomain structure of bcps, their macroscopic orientations have to be controlled. It may be most favorable to get a single crystal having a desired orientation in bulk bcp films. So far, in order to control the macroscopic orientations, external fields have been applied to bcps in the ordered state (e.g., shear[2−8] and electric fields[9,10]) or to bcps in the ordering process from disordered state (e.g., electric field[11,12] and light field[13]).

In this study, we impose a moving temperature gradient (∇T) to bcps during the ordering process from the disorder state, as an external field to control the macroscopic orientation of microdomains. We employed polystyrene-*block*-polyisoprene (SI) diblock copolymer (dibcp) forming hexagonally packed cylindrical microdomain structure (hex−cyl) in the ordered state in the absence of external fields. The principle of this method will be detailed in section 2.

Hashimoto and co-workers[14,15] for the first time applied this method of the so-called zone heating[16] to a lamella-forming dibcp bulk. They got a single crystal of lamella microdomain structure in the bulk film by imposing the moving ∇T as characterized by $\nabla T = 70$ °C/mm and moving rate $R = 25$ nm/s. The size of the single crystal obtained was 10 mm × 2 mm × 2 mm along O*x*, O*y*, and O*z* axes: the Cartesian coordinate will be defined later in conjunction with Figures 1, 2, 4, and 5. Moreover the unit vector normal to lamellar interface $\mathbf{n}_l$ is parallel to the direction of ∇T (O*z* axis) and the lamella edges were standing normal to the film surface (*xz* plane) all the way from top surface to bottom of the film.

Lamella microdomain structure has one-dimensional structure with a periodicity along one direction of $\mathbf{n}_l$ only. On the other hand, hex−cyl has a two-dimensional structure with a periodicity in the plane perpendicular to the cylinders axis, and its orientation is determined by orientation of unit vector parallel to cylinder axis ($\mathbf{n}_c$) and rotational angle around $\mathbf{n}_c$. In the one-dimensional structure of lamella, the moving ∇T controlled the lamellar orientation such that the lamella interfaces are normal to the vector of ∇T. It is quite intriguing to explore how the moving ∇T affects orientation of the two-dimensional system. Thus, in this paper we aim to explore this intriguing unknown problem.

2. Experimental Method

2.1. Sample. The samples used in this study were SI dibcp (SI-1) and homo-polyisoprene (HI). The dibcps were prepared by a sequential living anionic polymerization with *sec*-butyllithium as an initiator and cyclohexane as a solvent. The characteristics of polymers are summarized in Table 1. We used the blended sample of SI-1 and HI with a blending ratio of SI-1/HI = 95/5 wt % as a specimen. The sample SI-1/HI(95/5) was mixed with antioxidant (Irganox1010) and cast from a homogeneous solution in toluene with a total polymer concentration of 10 wt % and then annealed in vacuum (120 °C, 8 h). The as-cast film had a hex−cyl of polystyrene (PS) block chains in the matrix of polyisoprene (PI) block chains and HI chains where HI is expected to be uniformly solubilized in the matrix.[19] The Bragg spacing corresponding to the lattice spacing of the (100) plane, D_{100}, is 22 nm determined by small-angle X-ray scattering (SAXS). This specimen had order−disorder transition (ODT) temperature (T_{ODT}) at 178 °C as will be detailed in section 3. The reason for blending HI and SI is to

* To whom correspondence should be addressed.
† Kyoto University.
‡ Japan Atomic Energy Agency.
§ Present address: R&D Center, Mitsui Chemicals, Inc., 580-32 Nagaura, Sodegaura, Chiba 299-0265, Japan.
# Present address: ASRC, JAEA.

10.1021/ma070404c CCC: $37.00
Published on Web 07/06/2007

Table 1. Characteristics of the Polymers Used in This Work[a]

code	M_n	M_w/M_n	f_{PS}	T_{ODT} (°C)
SI-1	3.1×10^4	1.01	0.33	191
HI	1.2×10^3	1.08	0	
SI-1/HI(95/5)			0.31	178

[a] M_n: number-average molecular weight estimated by GPC, and M_w/M_n: polydispersity index where M_w is weight-average molecular weight measured by GPC. f_{PS}: volume fraction of polystyrene estimated by GPC ($f_{PS} = C\upsilon_{PS}/(\upsilon_{PS} + \upsilon_{PI})$, where C is volume fraction of bcp (SI-1) in as-cast film, and υ_{PS} and υ_{PI} are volume occupied by 1 mol of PS and PI block chains of bcp at room temperature, respectively. υ_{PS} and υ_{PI} are calculated by following equation: $\upsilon_i = M_{n,i}/\rho_i$, where i indicates PS or PI, $M_{n,i}$ is number-average molecular weight of PS or PI block chains determined by GPC, and ρ_i is density of corresponding homopolymer.[17,18] T_{ODT}: order−disorder transition temperature evaluated by SAXS.

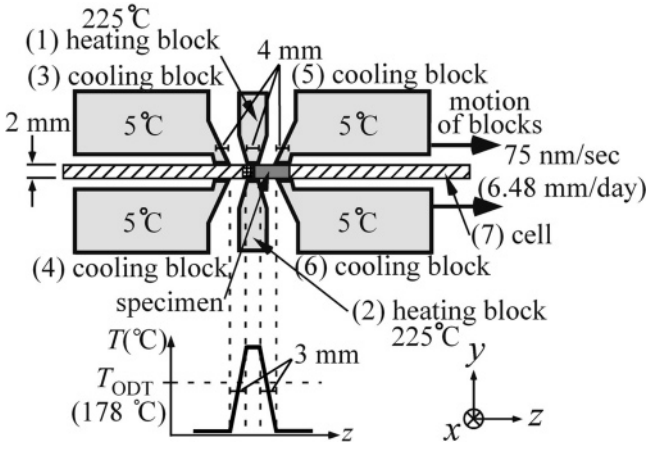

Figure 1. Schematic illustration of zone heating device used for imposing moving temperature-gradient field on specimen. The Cartesian coordination system defined as follows: O*z* is parallel to the temperature gradient axis, O*y* is parallel to the film normal, and O*x* is parallel to the film surface. The set of heating blocks [(1) and (2)] and cooling blocks [(3) to (6)] as a whole was slowly moved along the O*z* axis at a rate of 75 nm/s (6.48 mm/day), keeping the cell [(7)] at the fixed position.

enhance the scattering from the (110) plane of hex−cyl. This is necessary because the particular bcp SI-1 used in this work forms PS cylinder having a volume fraction such that its (110) scattering maximum is suppressed.[20] The absence of the maximum makes SAXS analyses of the hex−cyl with a special orientation developed under the zone heating method difficult. These characteristics will be detailed in section 3.

2.2. Zone Heating. We used a "zone heating device" as schematically shown in Figure 1. This device, described to some extent elsewhere,[14,15,21] consists of a pair of central heating blocks (parts 1 and 2), two pairs of cooling blocks (parts 3 and 4 plus parts 5 and 6), and a specimen cell (part 7). The central heating blocks were set in between the cooling blocks with their distance being adjustable (e.g., 3 mm in this experiment). The pair of heating blocks and the two pairs of cooling blocks are fixed together, and they move as a whole. They are aligned in such a way that a specimen in the specimen cell is placed exactly at the center of the blocks. The temperature of the heating blocks and that of the cooling blocks control a ∇T imposed on the specimen.

In this experiment, the heating blocks were set at 225 °C above the T_{ODT} (178 °C), while the cooling blocks to 5 °C well below the T_{ODT}. This arrangement produces a sharp nominal temperature gradient of $|\nabla T|_{nom} = 73$ °C/mm along the O*z* axis, which provides the external field for the ordering process of the specimens via ODT. The effective temperature gradient $|\nabla T|_{eff}$ was measured by measuring temperature at a given point with a thermocouple embedded in the specimen as a function of time for each moving rate R. Then the time change in temperature was converted into a positional (z) dependence of temperature by using a relationship of $z = Rt$. Thus, evaluated $|\nabla T|_{eff}$ was 42 °C/mm, much smaller

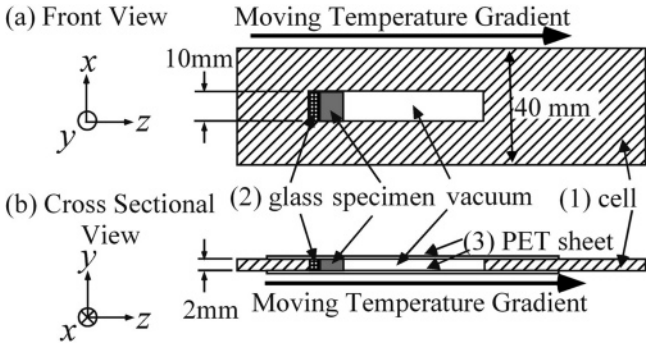

Figure 2. Schematic illustration of the cell used in zone heating device to hold the specimen: (a) top view and (b) cross-sectional view at its center. The film specimen was placed inside the cell made out of polytetrafluoroethylene (PTFE) [(1)] with a glass surface [(2)] on one end of the specimen surface along the O*z* axis and thin poly(ethylene terephthalate) (PET) sheets [(3)] on both side along the O*y* axis.

than $|\nabla T|_{nom}$, which may be due to conduction of heat within the specimen.

Figure 2 shows a detail of the specimen cell presented in Figure 1. The film specimen of 2 mm thickness and 10 mm width was placed inside the cell made out of polytetrafluoroethylene (PTFE) (part 1). A glass (part 2) was attached to the cell so that its surface perpendicular to the O*z* axis contacts with specimen at one end of the specimen surface. The specimen contacted with thin poly(ethylene terephthalate) (PET) sheets (part 3) on both sides of the specimen surface along the O*y* axis. Before the specimen is placed in the sample cell, the glass surface, the PTFE cell, and the PET sheets were cleaned with ethanol and dried in air.

The sample cell was fixed into the zone heating device. Then the set of heating blocks and cooling blocks as a whole was slowly moved along the O*z* axis at moving rate $R = 75$ nm/s (6.48 mm/day), keeping the cell at the fixed position as describe above. The motion of the set was controlled by a stepping motor: It intermittently moves the set at the rate 0.5 mm/s for the time 6×10^{-3} s in between a pause of 40 s. Thus, an averaged moving rate of the set is $R = 75$ nm/s. The entire zone heating device was kept under vacuum in order to prevent the specimen from thermal degradation. Moreover, the device was put on an air suspension vibration isorator (AG-1007, Meiritsu-Seiki Corp., Yokohama, Japan) in order to prevent the specimen from vibration along the O*y* direction. The slow motion of the set of the heating and cooling blocks imposes the slow moving ∇T on the specimens. The moving rate set to be the slowest velocity by the trial-and-error method in the range where thermal degradation of the specimen is effectively insignificant. We quenched the specimen below T_g by dunking it into liquid N_2 in order to freeze the structure developed via the zone heating method.

At this stage it may be useful to present a principle of our zone heating method for controlling the macroscopic orientation of ordered structures of bcp melts. Figure 3 schematically shows a principle of the method. The ∇T zone (part 3 in Figure 3a) runs through the bcp sample (part 1 in Figure 3a) in contact with a glass plate (part 2 in Figure 3a) along the O*z* axis. The ∇T zone is attained with a pair of the heating block controlled at $T_1 > T_{ODT}$ and the cooling block controlled at $T_2 < T_{ODT}$. It is divided into two regions: α-region at $T < T_{ODT}$ and β-region at $T > T_{ODT}$. As shown in Figure 3b, the bcp melt on the right-hand side of the glass surface staying in region β is in the disordered state. After the glass surface passes through region α and a very narrow zone of the sample goes into region α (Figure 3c), the ordering of the sample starts only from the narrow zone close to the glass surface area under a strong influence of the glass surface. However, the other zone of the sample is forced to be in the disordered state. The glass surface-induced ordering in the narrow zone selects orientation of microdomains: Figure 3 depicts the case of the lamella-forming SI dibcp where bright and dark stripes represent respectively PS and PI lamellae with their $\mathbf{n}_l$ parallel to the O*z* axis.[14,15] Subsequently, the

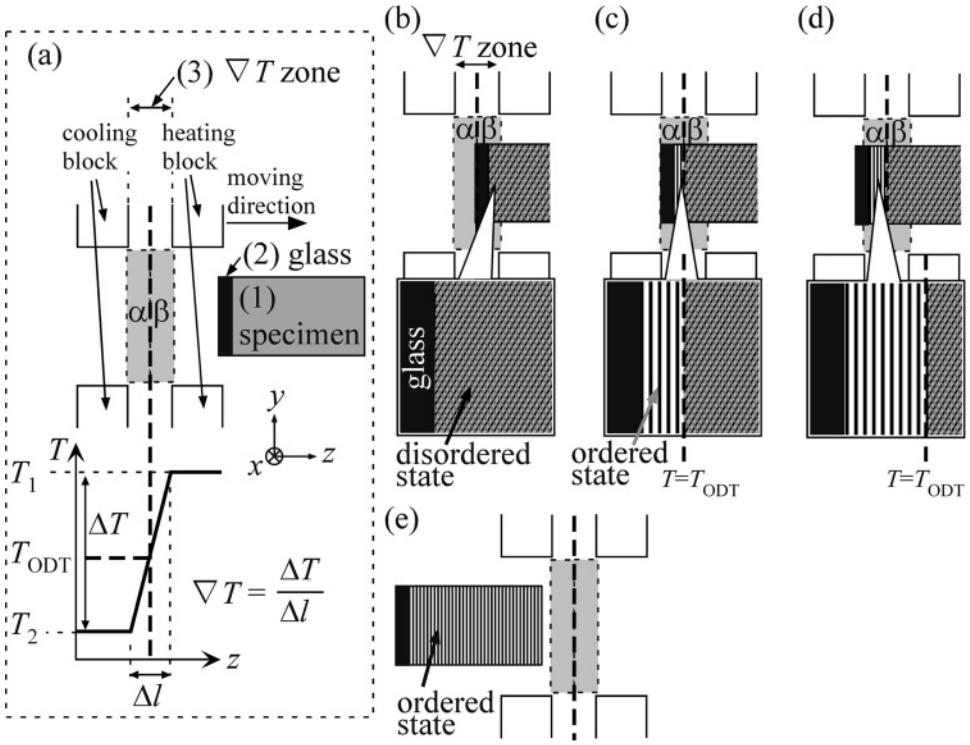

Figure 3. Schematic illustration of principle of the zone-heating method for lamella-forming block copolymer. (a) The temperature gradient from T_1 to T_2 moves from left to right keeping the specimen position fixed. As a result, temperature of sample can be lowered below T_{ODT} sequentially from the place that is near to glass surface to the place inside the specimen. This motion brings about a sequential ordering from the place that is near to glass surface (b) toward the interior of the specimen (e). The slow-moving rate and sharp temperature gradient suppress bulk nucleation from the region below T_{ODT}.

ordering front of specimen moves toward the moving direction of ∇T under the surface-induced ordering exerted by as-ordered, well-aligned microdomain structure, as shown in Figure 3d,e. During the growth, the well-aligned microdomain structure formed previously works as a new surface which controls the surface-induced ordering. By continuously moving the ∇T zone, the ordering sequentially occurs from the glass surface to the other end of specimen, and the macroscopically well-aligned microdomain structure is formed (Figure 3e).

In order to form a well-aligned microdomain structure, it is necessary that ∇T and its moving rate (R) are controlled to be large and small enough, respectively. Otherwise, a random nucleation and growth of microdomain may occur over a wide region of supercooled disordered melt. In the zone heating method, the ordering occurs in a restricted region having a finite width Δz_{order} ($\Delta z_{order} \equiv \Delta T_{order}/\nabla T$ with $\Delta T_{order} \equiv T_{ODT} - T_{g,PS}$ where $T_{g,PS}$ is glass transition temperature of PS microdomain) along the ∇T direction. If ∇T is too small, Δz_{order} becomes too large; that is, ordering occurs not only near the glass surface or the surface of as-ordered and well-aligned microdomain structure but also in the region away from the surface. Therefore, ordering without influence of the surface is allowed, and the resulting structure cannot have macroscopic orientation. Similary, if R is too large, the specimen in the ∇T zone cannot stay for a time enough to form surface-induced ordered structure, and a large area of the specimen is left undercooled state of disordered phase. The subsequent ordering from the undercooled disorder state results in the structure which is the same as that developed under conventionally quenched samples and is far from the well-aligned structure. Ideally, the value R should be smaller than the rate of surface-induced ordering.

2.3. Small-Angle X-ray Scattering. SAXS measurements were conducted for the specimens before and after application of the zone heating process. The specimens before the zone heating application was characterized by using an improved version of the laboratory-made SAXS apparatus.[22] It consists of a 18 kW rotating-anode X-ray generator (M18X HF by Bruker Co. Ltd., Japan) operated at 14 kW, a graphite crystal for incident beam monochromatization, a 2116 mm camera (705 mm from the source to the sample and 1411 mm from the sample to the detector) including two pinholes (0.5 and 0.5 mm) between the source and the sample, and a two-dimensional imaging plate (IP) detector.[23] The Cu Kα line ($\lambda = 0.154$ nm) was used as an incident beam. Exposure time for taking a SAXS pattern at the laboratory-made SAXS apparatus was 1 h.

The specimens after the zone heating were characterized using the synchrotron radiation small-angle X-ray scattering apparatus, as detailed elsewhere,[24] at the beamline 15A of the Photon Factory, Institute of Materials Structure Science, High Energy Accelerator Research Organization, Tsukuba, Japan. The wavelength (λ) of incident X-ray was 0.15 nm, and the spectral distribution $\Delta\lambda/\lambda$ was 10^{-3}. Two-dimensional (2D) SAXS images were obtained with a stage-mounted imaging plate (IP) system,[25] and the sample-to-detector distance was 2.3 m. The beam size at the sample surface was 0.5 × 0.5 mm.

We set the Cartesian coordinate Oxyz fixed to the specimen with its origin right in the middle of the glass surface which contacts with the specimen surface as shown in Figure 4. The specimen for SAXS measurement was cut out from the freezed, zone-heated specimen into a rectangular parallelepiped, as shown in Figure 4 (the specimen extends along Ox, Oy, and Oz directions, $-1.25 \le x/\text{mm} \le 1.25$, $-1.0 \le y/\text{mm} \le 1.0$, $0 \le z/\text{mm} \le 2.5$).

When Bodycomb et al.[14] applied the zone heating method to lamellar-forming bcps, they got the macroscopic single crystal of lamella with their interfaces perpendicular to the ∇T direction, and the lamellar edges standing perpendicular to the film surface. If we could get a similar macroscopic single crystal for the hex−cyl forming bcps also, the orientation of hex−cyl structure is expected to be independent of position along the Oz direction. Therefore, in order to clarify this point, the incident beam position was changed along the Oz direction, e.g., $z/\text{mm} = 0.3$, 0.9, 1.8, and 2.4 (Figure 5a), keeping $x = 0$ and keeping the incident beam irradiated along the Oy direction. Exposure time for taking a 2D SAXS pattern at each z position was 500 ms.

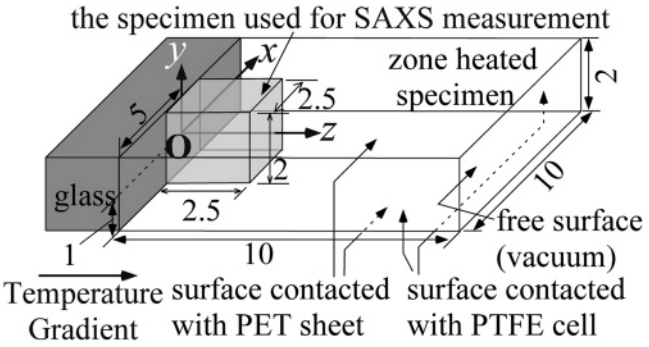

Figure 4. Schematic diagram showing the Cartesian coordinate O*xyz* fixed to the specimen with its origin right in the middle of the glass surface which contacts with the specimen surface. The lengths in this figure are expressed in unit of "mm". The specimen for SAXS measurement was cut out from the freezed, zone-heated specimen into a rectangular parallelepiped as described in transparent gray (the specimen extends along *x*, *y*, and *z* direction, $-1.25 \le x/\text{mm} \le 1.25$, $-1.0 \le y/\text{mm} \le 1.0$, $0 \le z/\text{mm} \le 2.5$).

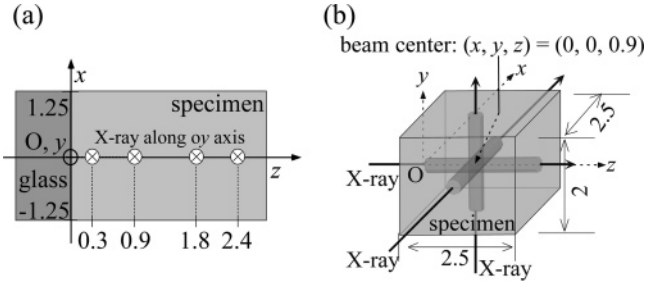

Figure 5. Schematic diagram indicating geometric relationship among incident X-ray beam, the specimen, and the Cartesian coordinate. The numbers are expressed in unit of "mm". In order to clarify the positional dependence of the orientation of hex−cyl along the *z* direction, the incident beam position was changed along the *z* direction, keeping $x = 0$ and $y = 0$ [(a)]. In order to clarify the orientation of hex−cyl, the incident X-ray beams were irradiated from three orthogonal directions along *x*, *y*, and *z* directions through a common center of (0, 0, 0.9) [(b)].

Next, in order to clarify the orientation of hex−cyl, the incident beam was irradiated from three orthogonal directions, along O*x*, O*y*, and Oz directions, through a common center of (0, 0, 0.9) (Figure 5b). Note that the sample thickness varies depending on the irradiation direction: 2.5, 2.0, and 2.5 mm along O*x*, O*y*, and Oz directions, respectively. Thickness (2 mm) along the O*y* direction is fixed by the specimen cell and is the optimum thickness of the specimen for the maximum scattering power which is determined by a balance of absorption coefficient of X-ray and scattering volume. The thickness (2.5 mm) along O*x* and Oz directions is also close to the optimum thickness of the sample. The thickness of 2.5 mm is almost the thinnest thickness that can be cut without distortions: The sample is too soft to be cut into a thinner thickness. There is a possibility that different local orientations are overlapped along the thickness direction of the incident beam path, as far as along O*x* and O*y* directions. However, the SAXS patterns along these directions are expected to be identical because there are no external fields along O*x* and O*y* directions, except for the surface of the PET sheet. The surface effect on the SAXS pattern taken with incident beam along the O*x* axis was not found because a part of the sample whose surface contacted to the cell were removed. The surface effect on the pattern taken with incident beam along the O*y* axis may exist, but this effect can be neglected as will be mentioned later in section 3. On the other hand, when the incident beam is irradiated along the Oz direction, there is no possibility that the overlapping effect of different orientations along this direction exists on the SAXS pattern, simply because there is no change in the orientation of hex−cyl along this axis, as will be mentioned later in section 3. Exposure time for taking a SAXS pattern along each direction was 500 ms.

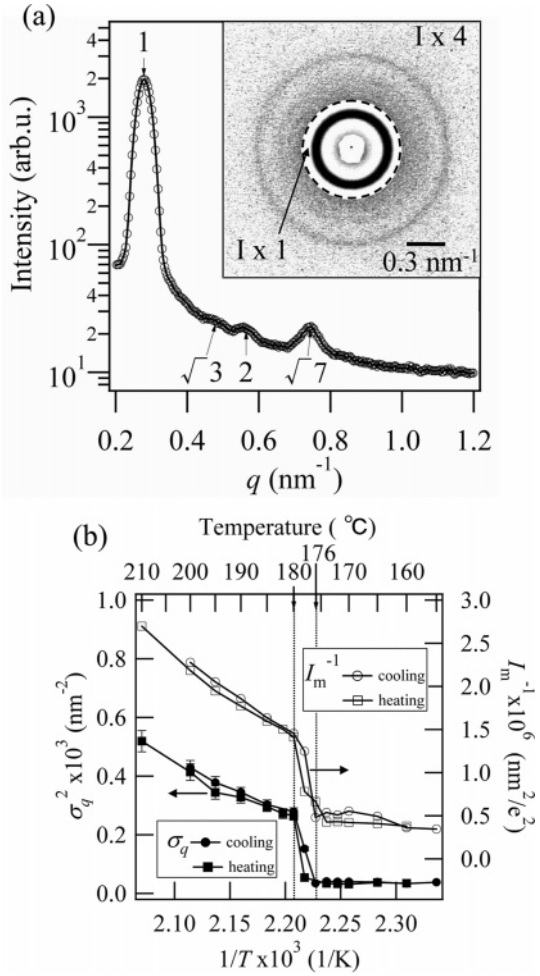

Figure 6. (a) Scattering profile obtained by a circular average of 2D-SAXS pattern for the specimen before zone heating. In the 2D-SAXS pattern shown in the inset the intensity outside of dashed line was multiplied by 4 times relatively to that inside the line. (b) The temperature dependence of the inverse maximum scattering intensity (I_m^{-1}) and square of the half-width at half-maximum (σ_q^2) of the 1st order peak as a function of the inverse absolute temperature ($1/T$). Measurements of cooling cycle from 200 to 155 °C were followed by those of heating cycle to 210 °C, and each measurement was done for 1 h after keeping at each temperature for 30 min.

3. Results

3.1. Characterization of Ordered Structure and ODT. Figure 6a presents the scattering profile obtained by a circular average of 2D-SAXS pattern (shown in the inset to Figure 6a) for the specimen before the zone heating. The 2D-SAXS pattern was recorded on the 2D imaging plate.[24] The profiles show four peaks at $q = q_m$, $\sqrt{3}q_m$, $2q_m$, and $\sqrt{7}q_m$ in Figure 6a, where q is the magnitude of scattering vector **q**, and q_m is the q value at maximum intensity. The peaks correspond to the diffraction maxima from the (100), (110), (200), and (210) plane of hex−cyl, respectively. We note that the peak at $\sqrt{3}q_m$ is still weak relative to those at $2q_m$ and $\sqrt{7}q_m$, even though the small amount of the homopolymer was added to enhance the scattering peak at $\sqrt{3}q_m$. We investigated temperature dependence of SAXS profiles of the specimen also in order to determine T_{ODT}. In Figure 6b the inverse maximum scattering intensity (I_m^{-1}) and square of the half-width at half-maximum (σ_q^2) of the peak at q_m are plotted as a function of the inverse absolute temperature

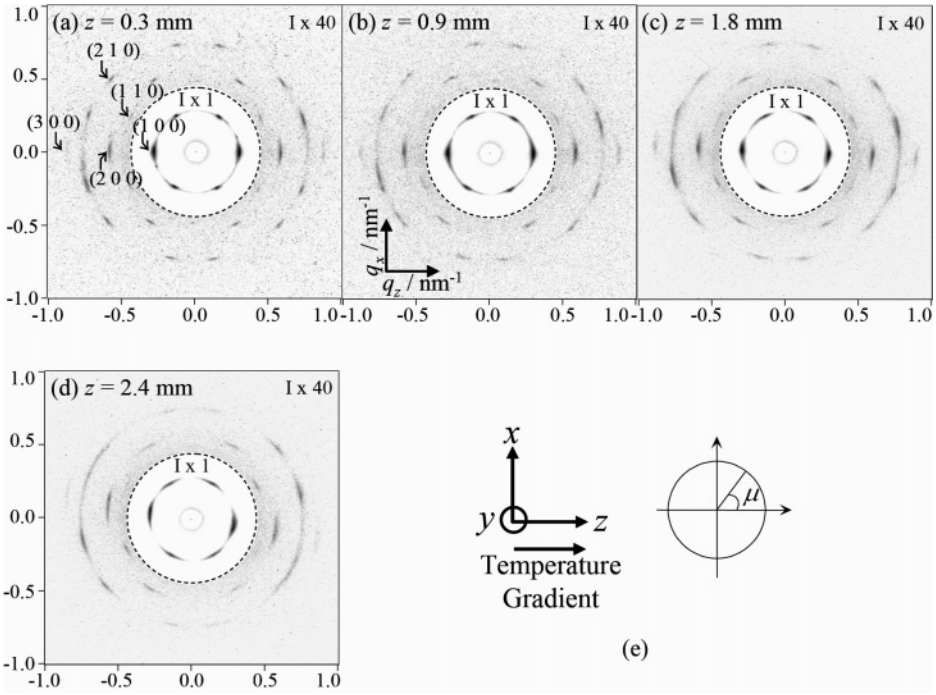

Figure 7. 2D-SAXS patterns obtained by irradiating incident X-rays parallel to the O*y* direction at a fixed position of $x = 0$ but by changing the irradiation point along temperature gradient direction (O*z* direction). The intensities outside of the circle drawn by the dashed line were multiplied by 40 times relatively to those inside the dashed line.

(1/*T*). The sharp discontinuous changes are observed in both I_m^{-1} vs 1/*T* and σ_q^2 vs 1/*T* at 176−180 °C, indicating that this sample has a sharp ODT, and its T_{ODT} is 178 ± 2 °C.

3.2. Positional Dependence of 2D-SAXS Patterns along Temperature-Gradient Direction. We explored the ordered structure developed under the zone heating method from a series of 2D SAXS pattern obtained by scanning the incident X-ray beam as a function of position and direction with respect to the specimens. First, as shown in Figure 5a, the incident beam was irradiated parallel to the O*y* direction at a fixed position of $x = 0$ but by changing the irradiation position along the O*z* direction, $z = 0.3$, 0.9, 1.8, and 2.4 mm. The corresponding patterns obtained are shown in Figure 7a−d, respectively.

Let us explain these SAXS patterns by choosing Figure 7a as an example. The lattice plane corresponding to each diffraction spot or maximum was specified from the *q* values at maximum intensities. The first-order scattering maximum from (100) plane gives the six-point pattern at azimuthal angle μ (defined in part e) equal to $\mu = 0°$, 60°, 120°, 180°, 240°, and 300°. Especially the two points along the O*z* direction ($\mu = 0°$ and 180°) are stronger than the others. The diffraction from the (200) and (300) plane naturally have the same characteristic as the (100) plane, though only a two-point pattern at $\mu = 0°$ and 180° is clearly visible for the diffraction from the (300) plane. The weak diffraction from the (110) plane gives the six-point pattern at $\mu = 30°$, 90°, 150°, 210°, 270°, and 330°, and they have almost the same intensity. The diffraction from the (210) plane gives the 12-point pattern at $\mu = 19.1°$, 40.9°, 79.1°, 100.9°, 139.1°, 160.9°, 199.1°, 220.9°, 259.1°, 280.9°, 319.1°, and 340.9°, and they also have almost the same intensity. The SAXS patterns b−d taken at other positions along the O*z* axis are essentially the same as pattern a, though the breadth of the maximum with respect to μ appears to slightly increase with *z*.

3.3. SAXS Patterns Taken with Incident Beam along O*x*, O*y*, and O*z* Axes. Since the SAXS pattern taken with incident beam parallel to O*y* axis was found to be almost independent of the position along the O*z* direction, we investigated a directional dependence of incident beam irradiation on the SAXS pattern at a fixed position along *z*, as shown in Figure 5b: X-rays were irradiated along O*x*, O*y*, and O*z* directions through a common center of (*x*/mm, *y*/mm, *z*/mm = 0, 0, 0.9). Parts a, b, and c of Figure 8 are the patterns observed in q_yq_z, q_xq_z, and q_xq_y planes taken with incident beam along O*x*, O*y*, and O*z* directions, respectively. Here q_x, q_y, and q_z are the *x*, *y*, and *z* component of scattering vector **q**.

The SAXS patterns in q_yq_z and q_xq_z planes have almost the same characteristics: they have the six-point pattern from the (100) plane with the two points along the O*z* direction having an enhanced intensity. The diffraction from the (200) plane have the same characteristic as the (100) plane. The diffraction from the (110) plane gives the six-point pattern, having almost the same intensity. The equality of the scattering patterns a and b is reasonable because the external field of the ∇T should induce "uniaxially symmetrical ordering" with respect to the O*z* axis: the ordered structure evolved should be identical in the plane perpendicular to the O*z* axis. This equality also indicates the fact that the PET sheets, which also contacted directly with the specimen surfaces normal to the *y*-axis, does not effectively affect orientation of hex−cyl. This is because if the PET sheets affects the orientation, they affect only the SAXS pattern taken with the incident beam parallel to *y*-axis but not the pattern taken with the incident beam parallel to *x*-axis, as the specimen surfaces normal to *x*-axis is free or at least very far from the PET sheets (see Figure 4), thereby giving rise to inequality of the patterns shown in Figure 8a,b. Figure 8a,b also implies a special orientation of hex−cyl evolved by the zone-heating method. Especially, the direction of the ∇T axis (O*z* axis) is shown to be a special direction because the two diffraction spots from the (100) plane along the q_z direction ($\mu = 0°$ and 180°) are stronger than those at other μ's.

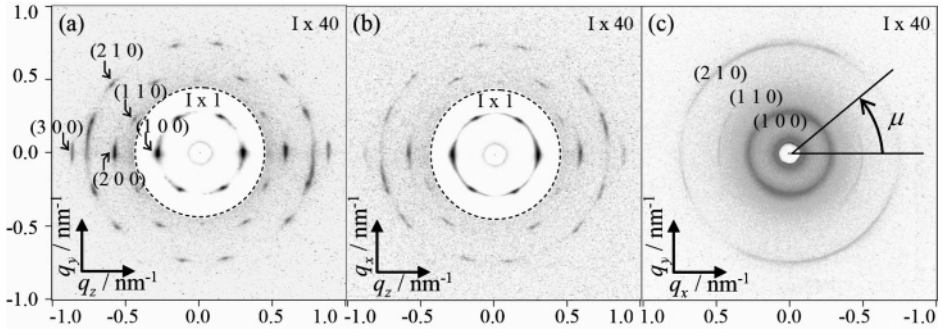

Figure 8. 2D-SAXS patterns obtained by irradiating X-rays along O*x*, O*y*, and O*z* directions through a common center of (*x*/mm, *y*/mm, *z*/mm = 0, 0, 0.9) [(a), (b), and (c), respectively]. The intensities outside of the circle drawn by the dashed line in q_yq_z plane (a) and q_xq_z plane (b), and in the all range of q in q_xq_y plane (c) was multiplied by 40 times relatively to those inside the dashed line in (a) and (b).

The SAXS pattern in Figure 8c is the pattern which reflects an average orientation of the hex−cyl structure developed along the O*z* axis from $z = 0$ to 2.5 mm. According to the result shown in section 3.2, however, there is no apparent positional dependence of the pattern with respect to the O*z* direction when the pattern is taken with incident beam along the O*y* direction (see Figure 7). Therefore, the SAXS pattern in the q_xq_y plane can reasonably represent true scattering free from the overlap effect along the O*z* axis. However, we should note that the SAXS pattern is an average over a finite area of the incident beam in the *xy* plane. Figure 8c shows diffraction from the (100), (110), and (210) plane of hex−cyl. They are almost independent of μ, indicating essentially uniaxial symmetry of the orientation of hex−cyl with respect to the ∇T direction. This result is consistent with the fact that the two patterns a and b in Figure 8 are equivalent.

4. Discussion

4.1. Orientation of Cylinders. (A) Positional Dependence of SAXS Patterns. As shown in Figure 7, the SAXS patterns with the incident beam along the O*y* axis were found to be independent of *z*, so that there are no significant changes in orientation of hex−cyl along the O*z* axis. In order to investigate more quantitatively the SAXS patterns, the azimuthal angle (μ) dependence of the diffraction from the (100) plane in each SAXS pattern was compared in Figure 9a. The results showed almost the same μ dependence at all *z* values investigated. The half-width at half-maximum of the peak at $\mu = 180°$ (σ_{180}) in Figure 9a is shown as a function of *z* in Figure 9b. There are almost no apparent *z* dependence except for a slight broadening at $z = 2.4$ mm. Therefore, the three SAXS patterns shown in Figure 8 taken with incident beam along the three orthogonal directions should represent the typical orientation of hex−cyl developed under the zone heating process.

(B) Directional Dependence of SAXS Patterns. We shall now analyze orientation of hex−cyl from the patterns shown in Figure 8. To quantitatively explore the SAXS patterns, the μ dependence of the diffraction from (100) plane in Figure 8a,b were compared and are shown in Figure 10a,b, respectively, while the μ dependence of the diffraction from the (100) and (110) plane in Figure 8c are shown in Figure 10c. The μ dependence in Figure 10a is essentially identical to that in Figure 10b, indicating that the two patterns in Figure 8a,b are quantitatively identical, both exhibiting the characteristics six-point patterns with enhanced intensity for the two points at $\mu = 0°$ and 180°. This piece of information together with such a piece of information that the (100) and (110) diffractions in the q_xq_y plane taken with incident beam along the O*z* axis are almost independent of μ give hints for visualization of the orientation of hex−cyl developed in this experiment.

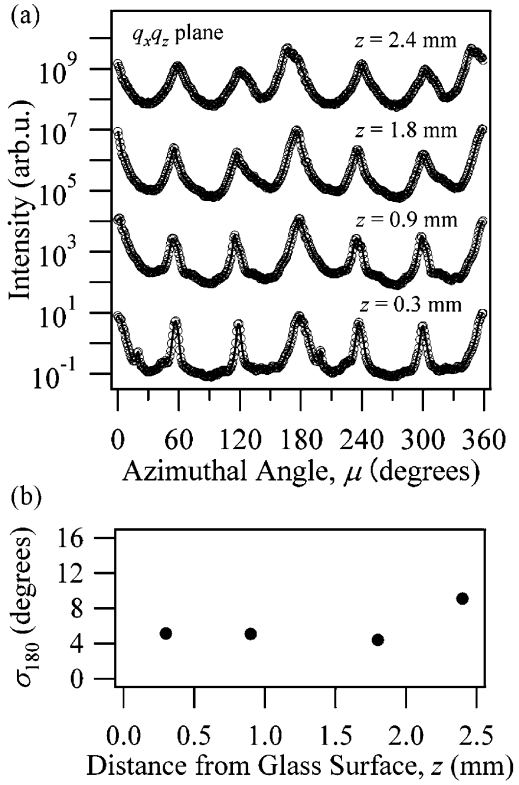

Figure 9. (a) The μ dependence of the scattering from the (100) plane in the 2D-SAXS patterns shown in Figure 7. The intensities of the data at *z*/mm = 0.3 are actual values, and those of other data were shifted up vertically by 3 decades relative to the intensities immediately below. (b) The *z* dependence of the half-width at half-maximum (σ_{180}) of the peak at $\mu = 180°$ in (a).

For the sake of convenience, a simplified pattern of Figure 8a is shown in Figure 11a, and a possible explanation for the pattern in Figure 11a is given by three models in Figure 11b, b-1 ($\phi = 90°$), b-2 ($\phi = 45°$), and b-3 ($\phi = 0°$), where ϕ is the rotational angle of cylinder axis around the O*z* axis in the plane of O*xy* (Figure 11c). These models indicate that one set of the (100) planes is perpendicular to the direction of the ∇T axis (O*z* axis), and there are some rotational freedom around the O*z* axis with respect to ϕ. The diffraction spot from the (100) plane is observed as the six-point pattern (spots A1−A6 in part a), which is consistent with model b-1 in Figure 11b.

Similarly, the diffraction spots from the (110) plane are observed as the six-point pattern (spots B1−B6 in part a). This

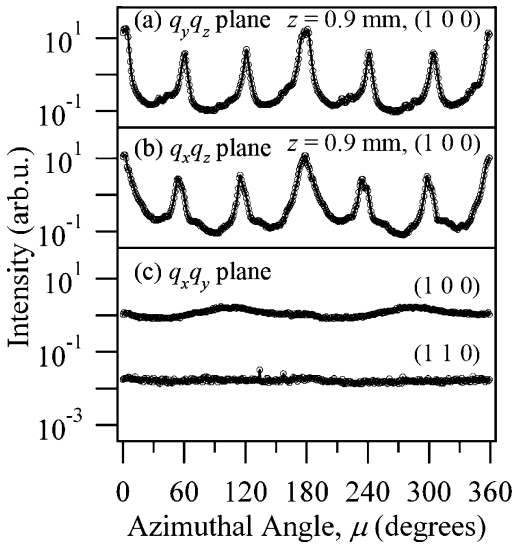

Figure 10. (a) and (b) are the μ dependences of the scattering from the (100) plane in 2D-SAXS patterns of parts a and b of Figure 8, respectively. (c) is the μ dependences of the scattering from (100) and (110) planes in the 2D-SAXS pattern of Figure 8c. In (c), the scattering intensity from the (100) plane is multiplied by 10.

also indicates the existence of model b-1 in Figure 11b. The weak intensity from the (110) plane is characteristic of this sample, SI-1/HI(95/5), as is also observed in Figure 6a before zone heating. Therefore, it is not due to either the disorder of orientation or distortion of hex−cyl. The diffraction from the (210) plane is the 12-point pattern (spots C1−C12 in part a). This is also consistent with model b-1 in Figure 11b.

Further, among the six points of (100) scattering, especially two points (A1 and A4) at $\mu = 0°$ and 180° along the Oz direction are stronger than the others. This indicates that the orientations of $\phi = 45°$ and 0° (models b-2 and b-3, respectively) in Figure 11b exist in addition to model $\phi = 90°$. Because of the contribution of the models with $\phi = 45°$ and 0°, the two points of the Oz direction are stronger than the other four points. We shall elucidate later that the rotation around the Oz axis is essentially uniform, giving rise to uniform distribution with respect to ϕ. The scattering from the (200) and (300) planes is the higher order diffraction of the (100) plane, and therefore they have the same charactaristics as the scattering from the (100) plane.

The same argument in Figure 8a is applied to Figure 8b, and the model shown in Figure 11b can explain the pattern in Figure 8b also. As mentioned in section 3, this is reasonable because the diffraction in the q_yq_z and q_xq_z plane should be equivalent.

Let us now discuss the diffraction pattern in Figure 8c. We should not overlook the very weak diffraction from the (110) plane. This diffraction is consistent with the models in Figure 11b, in which the (110) plane is parallel to the Oz direction. It is important to note that this diffraction is almost independent of μ, as clearly shown already in Figure 10, indicating that the rotational angle ϕ of cylinder axis with respect to the Oz axis is uniform.

An almost circular diffraction ring from the (100) plane is also observed in Figure 8c more clearly, although this cannot be explained by the model in Figure 11b. This indicates there is another possible orientation as shown in Figure 12 where three models, $\phi = 90°$ (a), $\phi = 45°$ (b), and $\phi = 0°$ (c), are presented, and ϕ is the angle already defined in Figure 11c. In the model of Figure 12, the (110) planes are perpendicular to the direction of the ∇T axis. If the orientation of Figure 11b is rotated by 30° around the cylinder axis, it becomes the orientation in Figure 12. In the models in Figure 12, the (100) plane is parallel to the Oz direction. Because of this orientation, the diffraction from the (100) plane is observed in Figure 8c. Moreover, the diffraction from the (100) plane is a circular ring, indicating ϕ takes uniformly from 0° to 180°, a uniform rotation of the cylinder axes around the Oz axis. The hex−cyl having this orientation is believed to be minor, simply because the six-point pattern from the (100) plane with maxima at $\mu = 30°$, 90°, 150°, 210°, 270°, and 330° are hardly visible in the patterns a and b in Figure 8.

An almost circular ring from the (210) plane is also observed in Figure 8c. This result is interpreted as a consequence of the fact that the models of Figure 11b have some rotational freedom around cylindrical axis. As shown in Figure 13, when the models of Figure 11b are rotated by ±10.9° around the cylinder axis, the (210) plane becomes parallel to the Oz direction, giving rise to the diffraction from the (210) plane. In fact, the μ dependence of the six-point pattern in Figure 8a,b or in Figure 10a,b suggests some rotational freedom around the cylinder axis.

4.2. Model for Hex−Cyl Texture Developed under Moving ∇T Field: "Columnar" Grains. Figure 14 schematically presents a model which is consistent with the three scattering patterns in Figure 8. Figure 14a presents the major orientation which corresponds to Figure 11b. In the major orientation, one set of the (100) planes is perpendicular to the ∇T direction and parallel to the glass surface; the cylinder axis is confined parallel to *xy* plane but is randomly oriented around the Oz axis; i.e., ϕ takes uniformly from 0° to 180° as evidenced by the results shown in Figure 8c or Figure 10c.

Considering the principle of ordering under the moving ∇T field, which involves glass-surface induced ordering and the domain growth along the Oz axis achieved by sequentially ordering from the region close to glass surface toward the interior of the specimen, it is anticipated that the grain having a fixed orientation of hex−cyl with respect to ϕ grows only along the Oz axis after an impingement of neighboring grains in the direction perpendicular to the *z*-axis, as shown in Figure 14b. We designate hereafter such grains as "columnar" grain for the sake of convenience from the viewpoint that the grain should have a shape extended along the Oz axis, though the grain shape is not necessarily columnar. In the initial stage of growth the grain grows both laterally (perpendicular to the Oz axis) and longitudinally (parallel to the Oz axis). The longitudinal growth is controlled by the slow moving rate of ∇T, and hence its growth rate is suppressed. On the other hand, the lateral growth is free from this suppression. Therefore, the grain is impinged to its neighboring grains in lateral directions before the front of the moving ∇T moves further along the *z* axis. The lateral grain size will be therefore controlled essentially by a number of nuclei formed parallel to the glass surface. On the other hand, the longitudinal growth of the grain is kept active as long as its growing front faces a sufficiently wide area of disordered phase. The arrow marked in the grain represents orientation of the cylinder axis (or director in the terminology of liquid crystals). The different grains have different director orientations, resulting in the uniform rotational angle ϕ.

Figure 14c represents the minor orientation of hex−cyl, which corresponds to Figure 12. In the minor orientation, one set of the (110) planes is perpendicular to the ∇T direction, and the rotation of the hex−cyl around the Oz axis and hence the angle ϕ is also uniform as is also evidenced by the results shown in Figure 8c or Figure 10c.

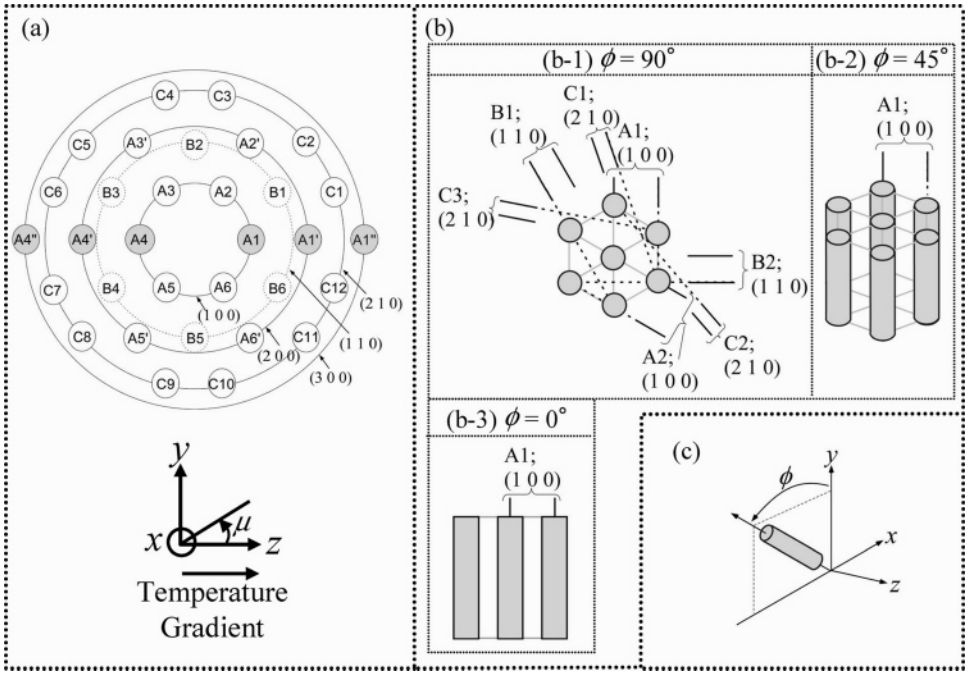

Figure 11. Schematic illustrations specifying the lattice plane corresponding to the each scattering spot in Figure 8a. (a) A simplified 2D-SAXS pattern of Figure 8a. (b) Hexagonally packed cylinder models explaining the 2D-SAXS pattern of part (a). Three models, $\phi = 90°$ (b-1), $\phi = 45°$ (b-2), $\phi = 0°$ (b-3), are presented, where ϕ is defined in (c). In all of these models, one set of the (100) planes is perpendicular to the direction of the temperature gradient axis (*z*-axis). The relationship between (a) and (b) is also described; e.g., the scattering spot marked as A1 in (a) corresponds to the (100) plane marked as A1 in (b). (c) The definition of ϕ which is the angle of cylinder axis in the plane of O*xy* for the rotation of the cylinder around the *z* axis. The Cartesian coordinate shown in part (a) is applied to the models in part (b) also.

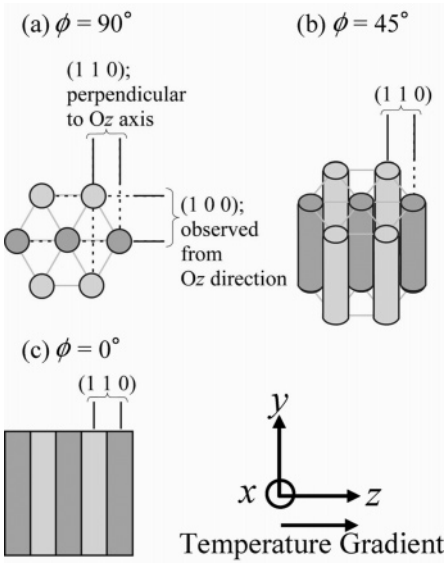

Figure 12. Hexagonally packed cylinder model which is different from the model in Figure 11b. Three models, $\phi = 90°$ (a), $\phi = 45°$ (b), $\phi = 0°$ (c), are tentatively presented, where ϕ is the angle already defined in Figure 11c. If the models of (b-1) to (b-3) in Figure 11b are rotated by 30° around the cylinder axis, they become the models of (a) to (c), respectively, in which one set of the (110) planes is perpendicular to the direction of the temperature gradient axis (*z* axis).

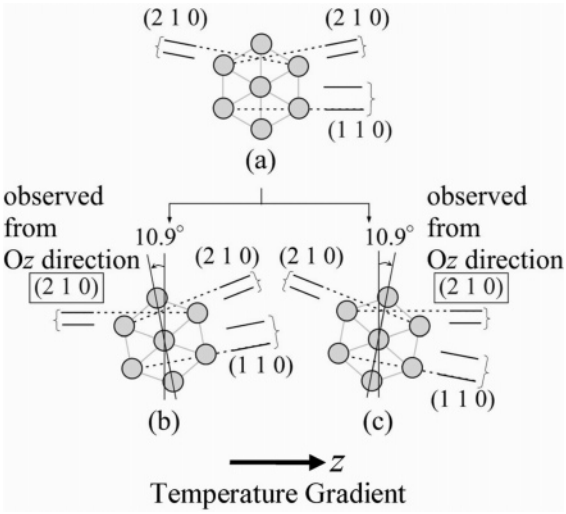

Figure 13. Schematic illustration of the models (b) and (c) explaining the diffraction from the (210) plane observed in Figure 8c. When the model of Figure 11b, which is represented by the model (a), is rotated by ±10.9° around the cylinder axis, the (210) plane becomes parallel to the Oz direction, giving rise to the diffraction from the (210) plane in the $q_x q_y$ plane.

We shall present a full real-space analysis of this system elsewhere[26] to confirm the model shown in Figure 14 and to further enrich information underlying the ordering mechanism driven by the moving temperature-gradient.

4.3. Relative Population of Major Orientation and Minor Orientation. In this section we shall analyze a relative population of the major orientation shown in Figure 14a and the minor orientation in Figure 14c. The major orientation and the minor orientation are different with respect to the rotational angle η around the cylinder axis by 30°: If the major orientation has $\eta = 0°$, then the minor orientation has $\eta = 30°$. Because both orientations take uniform rotational angle ϕ, the ratio of each orientation can be evaluated from the μ dependence of the (100) diffraction pattern taken with the incident X-ray beam along the O*x* and O*y* axes. Although it is conceivable that the real system has a distribution with respect to the angle η, we simplify our analysis by assuming that the distribution is given by a bimodal one having peaks at $\eta = 0°$ and 30°.

As described in conjunction with Figure 7a−d and Figure 8a,b in section 4.1, the major orientation shows six peaks in the μ dependence of the diffraction intensity from the (100) plane. They consist of two peaks at $\mu = 0°$ and 180°, which

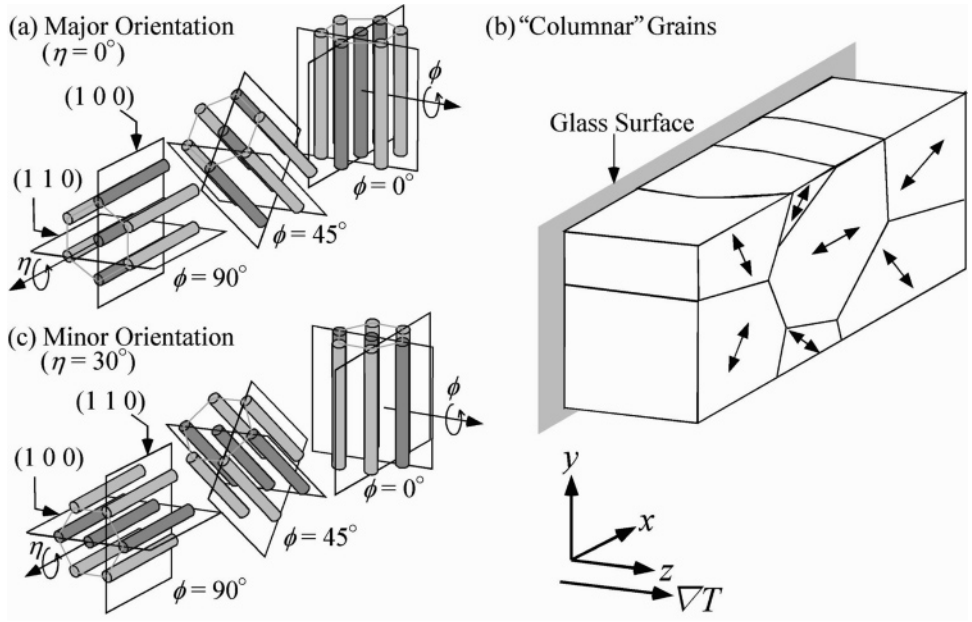

Figure 14. 3-dimensionnal models of the hex−cyl to explain the three scattering patterns in Figure 8 and columnar grains of hex−cyl. In major orientation (a), one set of the (100) planes is perpendicular to the direction of the temperature-gradient axis and parallel to the glass surface, and the cylinder axis in the *xy* plane is randomly rotated around the Oz axis; i.e., ϕ takes uniformly from 0° to 180°. It is anticipated that the grain having a fixed orientation of hex−cyl with respect to ϕ grows along *z*-axis into a columnar shape (b), where the arrow marked in the grain represents orientation of the cylinder axis. In minor orientation (c), the (110) planes are perpendicular to the direction of the temperature gradient axis and parallel to glass surface, and the direction of the cylinder axis in the *xy* plane is randomly rotated around the Oz axis; i.e., ϕ takes uniformly from 0° to 180°.

are the diffraction from the major orientation with the rotational angle ϕ from $\phi = 0°$ to 180° in Figure 14a and four peaks at $\mu = 60°$, 120°, 240°, and 300° which are the diffraction from major orientation having a specific value of ϕ in Figure 14a. The latter four peaks in the q_yq_z plane correspond to the diffraction from the model having $\phi = 90°$ in Figure 14a, while those in the q_xq_z plane correspond to the diffraction from the model having $\phi = 0°$ in Figure 14a. The (100) diffraction from the minor orientation has six peaks at $\mu = 30°$, 90°, 150°, 210°, 270°, and 330° in the q_yq_z plane and in the q_xq_z plane, which correspond to the diffraction from the model having $\phi = 90°$ and $\phi = 0°$ in Figure 14c, respectively. Therefore, the population of each orientation can be evaluated by comparing the intensities of the diffraction peaks corresponding to major orientation with those corresponding to minor orientation.

In the real data, each intensity at $\mu = 30°$, 90°, 150°, 210°, 270°, and 330° contains not only the contribution of the peak intensity corresponding to the minor orientation but also the contribution of the tail intensity of the strong diffraction peaks corresponding to the major orientation. Nevertheless, we ignored the contribution of the tail intensity to the peak diffraction intensity from the major orientation for our qualitative evaluation of the relative population of the major and minor orientations. Therefore, we directly compare the intensities at $\mu = 60°$, 120°, 240°, and 300° in the q_yq_z plane and the q_xq_z plane, which reflect the population of major orientation, with those at $\mu = 90°$ and 270° in the q_yq_z plane and the q_xq_z plane, which reflect the population of minor orientation, respectively (see Figure 9a as well as Figure 10a,b). In order to minimize the contribution of the tails of the strongest peaks at $\mu = 0°$ and 180°corresponding to major orientation, we chose intensities at $\mu = 90°$ and 270° from the intensities at the six azimuthal angles corresponding to the minor orientation.

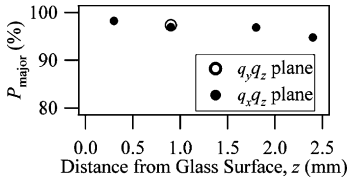

Figure 15. *Z* dependence of the weight fraction of major orientation (P_{major}). P_{major} was calculated using the μ dependence of the diffraction intensity from the (100) plane in each SAXS pattern of Figure 7a−d (q_xq_z plane), which is shown in Figure 9a, and Figure 8a (q_yq_z plane) which is shown in Figure 10a.

The weight fraction of major orientation P_{major} in percent (%) is thus calculated:

$$P_{major} = \bar{I}_{major}/(\bar{I}_{major} + \bar{I}_{minor}) \times 100 \qquad (1)$$

$\bar{I}_{major}$ is the averaged intensities of each peak at $\mu = 60°$, 120°, 240°, and 300° corresponding to the major orientation, and $\bar{I}_{minor}$ is the averaged intensities at $\mu = 90°$ and 270° corresponding to the minor orientation.

P_{major} was calculated using the μ dependence of the diffraction intensity shown in Figure 9a (q_xq_z plane) and Figure 10a (q_yq_z plane) and plotted as a function of the distance *z* from the glass surface in Figure 15. All of the values of P_{major} are in the range from 95% to 98%, slightly decreasing with *z*. P_{major} estimated in the q_yq_z plane (open circle) was found to be in a good agreement with that q_xq_z plane (filled circle) at $z = 0.9$ mm.

4.4. Glass Surface-Induced Orientation and Effect of Moving Temperature Gradient. (A) Surface-Induced Ordering. In this section we discuss about the glass-surface induced orientation and effect of moving ∇T. It is likely that PS block chains selectively wets to the interface between the bcp and glass surface because the PS block is much polar than PI block. This selective wetting can be also confirmed by comparing the interfacial tension between PS and glass ($\gamma_{PS-glass}$) with that

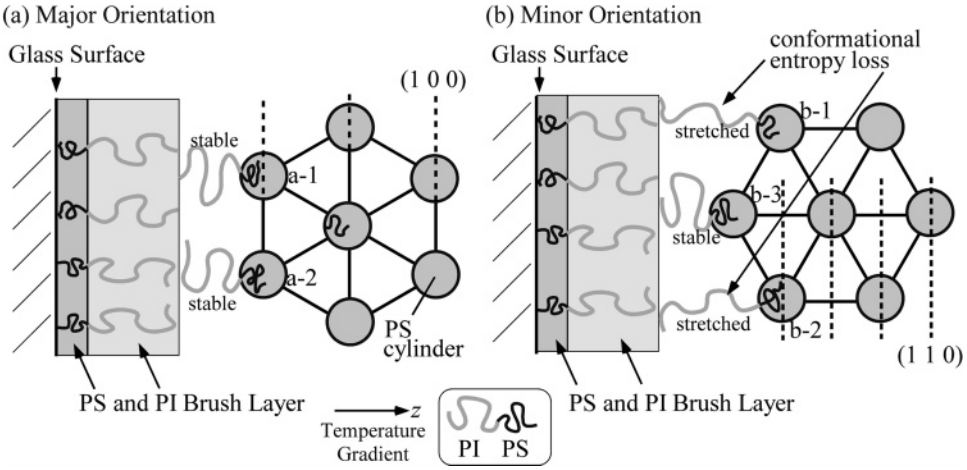

Figure 16. Schematic illustrations indicating packing of the bcp chains on the glass surface for both major orientation (a) and minor orientation (b). The selective wetting of PS block chains on the glass surface may generate a brush layer of PS and PI block chains on the glass side and the interior side, respectively. All the PI corona chains which emanate from PS cylinders (a-1, a-2, b-1 to b-3, etc.) are expected to contact to PI brush layer in order to reduce the interfacial tension between the PI corona chain and the glass surface. The penalty of conformational entropy loss of PI corona chains is smaller in the major orientation than in minor orientation, which causes the model (a) in dominant than model (b).

between PI and glass ($\gamma_{PI-glass}$). These interfacial tensions are expressed as follows:[27]

$$\gamma_{P-glass} = \gamma_P + \gamma_{glass} - 2(\gamma_P{}^d\gamma_{glass}{}^d)^{1/2} - 2(\gamma_P{}^p\gamma_{glass}{}^p)^{1/2} \quad (2)$$

where P indicates either PS or PI. γ_P and γ_{glass} are the surface tension of polymer (PS or PI) and glass against air, respectively. $\gamma_P{}^d$ and $\gamma_{glass}{}^d$ are dispersion component of γ_P and γ_{glass}, while $\gamma_P{}^p$ and $\gamma_{glass}{}^p$ are the polar component of γ_P and γ_{glass}, respectively. γ_{glass}, $\gamma_{glass}{}^d$, and $\gamma_{glass}{}^p$ were reported.[27] γ_P, $\gamma_P{}^d$, and $\gamma_P{}^p$ were also reported[27] or can be calculated from the reported value.[28,29] Therefore, $\gamma_{PS-glass}$ and $\gamma_{PI-glass}$ can be calculated as follows: $\gamma_{PS-glass} = 149$ (from ref 28) to 175 mJ/m^2 (from ref 27), while $\gamma_{PI-glass} = 186$ and 195 mJ/m^2 for *trans*- and *cis*-PI, respectively (from ref 29). In any case $\gamma_{PS-glass}$ is smaller than $\gamma_{PI-glass}$. Therefore, PS block chains selectively wets to the interface between the bcp and the glass.

Figure 16 schematically indicates a possible packing of polymer chains on the glass surface for both major orientation (a) and minor orientation (b). This is similar to the surface-induced ordering in very thin film.[30−33] The selective wetting of PS block chains on the glass surface may generate a brush layer of the bcps composed of a layer of PS and a layer of PI block chains in the glass side and in the interior side across the interface, as illustrated by Figure 16. In this way PI block chains forming the matrix phase of PS cylinders contact with PI brushes formed on the glass surface to minimize the interfacial energy. Without the brush layer, the PI block chains emanating from PS cylinders must directly contact with glass surface, hence encountering unfavorable interactions between the glass and the PI.

(B) Selection of Orientation. We now discuss a physical origin of the major and minor orientation. For the discussion we may focus on the cost of conformational entropy loss of PI chains, which emanate from the cylinders a-1 and a-2 in part a and b-1 to b-3 in part b in Figure 16, in order to fill the intervening space between the PI brush layer adhered on the glass and the surface of the hex−cyl domain under the demand of incompressibility. We may qualitatively anticipate the penalty is smaller in the major orientation (a) than the minor orientation (b). This is because if the PI chains from the cylinder (b-3) in the minor orientation are in favorable conformations, then those from the cylinders (b-1) and (b-2) must have stretched conformations; if the PI chains from the cylinders (b-1) and (b-2) are in favorable conformations, then those from (b-3) must have compressed conformations. Such a penalty of conformational entropy is less encountered in the case of the major orientation.

(C) Comments on Effects of ∇T and Moving Rate. The value $|\nabla T|_{eff}$ of 42 °C/mm employed in this work corresponds to 9.2×10^{-4} °C/D_{100}, and the moving rate $R = 75$ nm/s corresponds to $3.4D_{100}$/s, by using experimental result of $D_{100} = 22$ nm. One may think that the ∇T of 1.8 mK/($2D_{100}$) is too small to orient the microdomain structure. If thermal correlation length ξ of bcp near ODT is of the order of 20 times $2D_{100}$, then the ∇T is 36 mK/ξ. This corresponds to a situation that the region having undercooling below T_{ODT} by 0.1 °C extends over the space of $2.7\xi = 108D_{100}$. Thus, the ∇T may not be large enough. This weak point may be overcome by the slow moving rate of $3.4D_{100}/s = 0.085\xi/s$. The latter may be effective in creating the moving-∇T-induced orientation of hex−cyl (the columnar grain of hex−cyl).

We may offer another scenario for the ∇T -induced orientation of hex−cyl as follows. It is not always necessary that the ordering occurs in the very narrow slitlike space (of the thickness of order of $2D_{100}$) at the interface of ordered phase and disordered phase. Even if new nucleation of hex−cyl (designated here after as "new" grains) occurs at a place in the disorder melt which is slightly away from the interface of order phase and disorder phase, the "as-grown" grain having glass-surface induced orientation can grow via a "matched coalescence" with the "new" grains; the new grains which are generated due to the nucleation have freedom to rotate and adjust its orientation to that of "as-grown" grain. In this process the moving rate of ∇T is still important because the time sufficient to adjust the orientation of "new" grain to that of "as-grown" grain is necessary.

5. Concluding Remarks

The couple of moving ∇T field and surface-induced ordering field imposed on the ordering process of cylinder-forming block copolymer from disordered melt was discovered to develop a unique texture of hex−cyl as summarized in the Abstract. The most important feature in the texture developed under this

external field is that the ∇T field orients the cylinder axis normal to the temperature gradient direction (∇T axis) with complete rotational freedom of cylinder axis around the ∇T axis. The more specific features of the texture were summarized in the Abstract and detailed in section 4.2 in conjunction with Figure 14.

Acknowledgment. A part of the SAXS measurements in this work was conducted under approval of the Photon Factory Advisory Committee (2002G204). This research is partially supported by Japan Society for the Promotion of Science, Grant-in-Aid for Scientific Research (C), 19550206, and Grant-in-Aid for Scientific Research (S), 17105004.

References and Notes

(1) Khandpur, A. K.; Förester, S.; Bates, F. S.; Hamley, I. W.; Ryan, A. J.; Bars, W.; Almdal, K.; Mortensen, K. *Macromolecules* **1995**, *28*, 8796.
(2) Koppi, K. A.; Tirell, M.; Bates, F. S.; Almdal, K.; Colby, R. H. *J. Phys. II* **1992**, *2*, 1941.
(3) Winey, K. I.; Patel, S. S.; Larson, R. G.; Watanabe, H. *Macromolecules* **1993**, *26*, 2542.
(4) Okamoto, S.; Saijo, K.; Hashimoto, T. *Macromolecules* **1994**, *27*, 5547.
(5) Winter, H. H.; Scott, D. B.; Gronski, W.; Okamoto, S.; Hashimoto, T. *Macromolecules* **1993**, *26*, 7236.
(6) Jackson, C. L.; Barnes, K. A.; Morrison, F. A.; Mays, J. W.; Nakatani, A. I.; Han, C. C. *Macromolecules* **1995**, *28*, 713.
(7) Okamoto, S.; Saijo, K.; Hashimoto, T. *Macromolecules* **1994**, *27*, 3753.
(8) Shin, G.; Sakamoto, N.; Saijo, K.; Suehiro, S.; Hashimoto, T.; Ito, K.; Amemiya, Y. *Macromolecules* **2000**, *33*, 9002.
(9) Amundson, K.; Helfand, E.; Quan, X.; Smith, S. D. *Macromolecules* **1993**, *26*, 2698.
(10) Amundson, K.; Helfand, E.; Quan, X.; Hudson, S. D.; Smith, S. D. *Macromolecules* **1994**, *27*, 6559.
(11) Amundson, K.; Helfand, E.; Davis, D. D.; Quan, X.; Patel, S. S.; Smith, S. D. *Macromolecules* **1991**, *24*, 6546.
(12) Thurn-Albrecht, T.; DeRouchey, J.; Russell, T. P.; Jaeger, H. M. *Macromolecules* **2000**, *33*, 3250.
(13) Travasso, R. D. M.; Kuksenok, O.; Balazs, A. C. *Langmuir* **2006**, *22*, 2620.
(14) Hashimoto, T.; Bodycomb, J.; Funaki, Y.; Kimishima, K. *Macromolecules* **1999**, *32*, 952.
(15) Bodycomb, J.; Funaki, Y.; Kimishima, K.; Hashimoto, T. *Macromolecules* **1999**, *32*, 2075.
(16) Anthony, R. W. *Solid State Chemistry and its Application*; John Wiley & Sons: New York, 1984.
(17) Furuta, I.; Kimura, S.; Iwama, M. In *Polymer Handbook*, 4th ed.; Brandrup, J., Immergut, E. H., Grulke, E. A., Eds.; John Wiley & Sons: New York, 1999; p V-6.
(18) Schrader, D. In *Polymer Handbook*, 4th ed.; Brandrup, J., Immergut, E. H., Grulke, E. A., Eds.; John Wiley & Sons: New York, 1999; p V-91.
(19) Hashimoto, T.; Tanaka, H.; Hasegawa, H. *Macromolecules* **1990**, *23*, 4378.
(20) Hashimoto, T.; Kawamura, T.; Harada, M.; Tanaka, H. *Macromolecules* **1994**, *27*, 3063.
(21) Funaki, Y.; Bodycomb, J. Japanese Patent application H9-140196 (assigned to ERATO, JST, and Daicell Co.).
(22) Hashimoto, T.; Suehiro, S.; Shibayama, M.; Saijo, K.; Kawai, H. *Polym. J.* **1981**, *13*, 501.
(23) Hashimoto, T.; Okamoto, S.; Saijo, K.; Kimishima, K.; Kume, T. *Acta Polym.* **1995**, *46*, 463.
(24) Amemiya, Y.; Wakabayashi, K.; Hamanaka, T.; Wakabayashi, T.; Matsushita, T.; Hashizume, H. *Nucl. Instrum. Methods* **1983**, *208*, 471.
(25) Suehiro, S.; Saijo, K.; Seto, T.; Sakamoto, N.; Hashimoto, T.; Ito, K.; Amemiya, Y. *J. Synchrotron Radiat.* **1996**, *3*, 225.
(26) Mita, K.; Takenaka, M.; Hasegawa, H.; Hashimoto, T. Manuscript in preparation.
(27) Kinloch, J. *Adhesion and Adhesives*; Chapman and Hall: London, 1987.
(28) Wu, S. In *Polymer Handbook*, 4th ed.; Brandrup, J., Immergut, E. H., Grulke, E. A., Eds.; Wiley: New York, 1999; p VI-525.
(29) Lee, L. H. *J. Polym. Sci., Part A-2: Polym. Phys.* **1967**, *5*, 1103.
(30) Huinink, H. P.; Brokken-Zijp, J. C. M.; van Dijk, M. A.; Sevink, G. J. A. *J. Chem. Phys.* **2000**, *112*, 2452.
(31) Huinink, H. P.; van Dijk, M. A.; Brokken-Zijp, J. C. M.; Sevink, G. J. A. *Macromolecules* **2001**, *34*, 5325.
(32) Radzilowski, L. H.; Carvalho, B. L.; Thomas, E. K. *J. Polym. Sci., Part B: Polym. Phys.* **1996**, *34*, 3081.
(33) Karim, A.; Singh, N.; Sikka, M.; Bates, F. S.; Dozier, W. D.; Felcher, G. P. *J. Chem. Phys.* **1994**, *100*, 1620.

MA070404C